Journal of Sound and Vibration (1997) **199**(3), 473–489

A RADIATION EFFICIENCY FOR UNBAFFLED PLATES WITH EXPERIMENTAL VALIDATION

C. H. Oppenheimer† and S. Dubowsky

Department of Mechanical Engineering, M.I.T., Cambridge, MA 02139, *U.S.A.*

(*Received* 7 *July* 1995, *and in final form* 1 *July* 1996)

A radiation efficiency is developed for sound radiation from rectangular plates with unbaffled edges below the plate critical frequency. The expression modifies the modal average radiation efficiencies obtained from the simply supported plane-baffled plate by considering the effects of fluid flow around a structure. These flows reduce sound radiation by allowing fluid to escape compression. The unbaffled plate radiation efficiency is assessed by comparison with experimental data of sound radiated by impacts between balls and a plate. The expression is observed to be more accurate than the simply supported plane-baffled plate model and more versatile than a model of sound radiated from a plane-baffled free edge of a plate. Sound radiated by non-propagating plate vibration near ball-plate impacts appears to play a minor role. Improvements in accuracy over the simply supported plane-baffled model typically range from 4–12 dB, with the greatest improvements occurring at low frequencies. A statistical method for bounding radiated sound power with a degree of confidence is also developed and tested against measured data. The results are encouraging but not statistically conclusive due to a limited amount of measured data.

1. INTRODUCTION

Substantial research has addressed the important problem of sound radiation from plates [1–6]. Plate acoustics are often described in terms of radiation efficiencies, which relate radiated sound power to spatially averaged vibration [7]. Using a simply supported plane-baffled plate model, radiation efficiencies have been derived for both individual plate modes and sets of plate modes [1, 8, 2, 9, 3]. The latter are called modal average radiation efficiencies and are obtained by assuming that plate modes resonate with equal energy [1, 8].

The plate critical frequency has been identified as an important parameter [1, 10]. Sound with frequencies above critical is radiated efficiently and depends largely on the area and the space-averaged square of surface velocity [1, 8]. Sound with frequencies below critical is radiated less efficiently [1, 10], and depends largely on the spatial distribution of vibration near structural discontinuities such as the plate perimeter or stiffeners [11, 12], and neighboring structures which baffle the plate [13].

Various descriptions of these low frequency phenomena have been developed. These include representations of the effects of stiffeners [1], neighboring structures [13], free boundary conditions [14], and oscillating inertial flows surrounding a plate at low frequencies where the acoustic wavelength exceeds plate dimensions [15]. A correction to describe the effect of radiation-reducing inertial flows occurring in a localized region near the edges of unbaffled plates at higher frequencies has not been developed, although a

† Currently at Engineering Technology Center, Arlington, VA 22202, U.S.A.

0022–460X/97/030473 + 17 $25.00/0/sv960609

means for obtaining such a correction was suggested [16]. An iterative numerical method has also been used to compute sound radiation from unbaffled plates [17].

In this paper a radiation efficiency for unbaffled rectangular plates is developed for frequencies below the plate critical frequency. In developing the expression, radiating sources near the plate perimeter are represented by oscillating spheres and cylinders as suggested in reference [16]. The unbaffled plate radiation efficiency contains newly derived local corrections that account for the effects of localized inertial flows near the edges of unbaffled plates and is presented in Section 2. The unbaffled plate radiation efficiency also contains a plate correction similar to that of reference [15] to represent the effects of inertial flows that envelop a plate at low frequencies. The local and plate corrections both contain scaling factors which are obtained empirically by comparison with measured data reported in previous work [18]. The unbaffled plate radiation efficiency is assessed in Section 3 by comparison against this data and predictions by existing models, namely the simply supported baffled plate model and a model of sound radiation from baffled plate edge with a free boundary condition [14]. The unbaffled expression is then assessed further using measurements of sound power radiated by balls impacting a plate in Section 4. Predictions by the baffled-supported and baffled-free plate radiation models, as well as a model of sound radiated by non-propagating plate vibration near ball-plate impact points, are compared to the measured data and the unbaffled radiation efficiency. A method for bounding sound power with a degree of certainty is also presented in Section 4 which is based on reference [19].

2. A RADIATION EFFICIENCY FOR UNBAFFLED PLATES

2.1. BACKGROUND

Radiation efficiency σ is defined as the proportionality between radiated sound power Π and the square of surface normal velocity $\langle v^2 \rangle$ averaged over time and radiating surface S:

$$\Pi = \sigma \rho_o c S \langle v^2 \rangle, \tag{1}$$

in which ρ_o is the density of the acoustic fluid, and c is the speed of sound. A radiation efficiency for frequencies below the plate critical frequency has been developed by averaging radiation efficiencies of the modes of a simply supported plane-baffled plate [1, 2]. In this paper this expression is called the (subcritical) baffled plate radiation efficiency:

$$\sigma_{baf} = \sigma_{corner} + \sigma_{edge}, \qquad f < f_c, \tag{2}$$

in which σ_{corner} and σ_{edge} are the modal average radiation efficiences for the so-called corner and edge modes, and f_c is the critical frequency of the plate. Corner modes radiate primarily from regions near the corners of a plate (see Figure 1), and edge modes radiate primarily from regions along the plate perimeter [1]. The σ_{corner} and σ_{edge} are given by [1]

$$\sigma_{corner} = \frac{8}{\pi^4}\left(\frac{\lambda_c^2}{A}\right) \times \begin{cases} (1 - 2\alpha^2)/(\alpha(1 - \alpha^2)^{1/2}), & \alpha^2 < 1/2, \\ 0, & \alpha^2 \geqslant 1/2, \end{cases} \tag{3}$$

$$\sigma_{edge} = \frac{1}{4\pi^2}\left(\frac{P\lambda_c}{A}\right)\left[\frac{(1 - \alpha^2)\ln((1 + \alpha)/(1 - \alpha)) + 2\alpha}{(1 - \alpha^2)^{3/2}}\right], \tag{4}$$

in which A = area of one side of a plate, P = plate perimeter, $\alpha = (f/f_c)^{1/2}$ where f is frequency and f_c is plate critical frequency, and λ_c = acoustic wavelength at the plate critical frequency.

The expression in equation (3) was originally presented in reference [1] and has been corrected in reference [20]. The radiation efficiency of equation (2), based on a simply supported model with an infinite plane baffle, cannot accurately model sound radiation at low frequencies where the plate is unbaffled, or surrounding structures serve as non-plane acoustic baffles and affect sound radiation [1, 16]. The radiation efficiency introduced in the next section overcomes this limitation for unbaffled plates which have no surrounding structures through the use of oscillating spherical and cylindrical sources, as shown in Figure 1.

2.2. A SUBCRITICAL RADIATION EFFICIENCY FOR UNBAFFLED PLATES

The subcritical radiation efficiency σ_{unb} presented in this paper is intended for sound radiation below the critical frequency of rectangular unbaffled plates. In the development it is assumed that the plate edges are simply supported and that sound is radiated primarily by resonating plate modes that vibrate with equal energies, as has been done to obtain the modal average radiation efficiencies σ_{corner} and σ_{edge} in equation (2). Unlike equation (2), however, the unbaffled plate radiation efficiency is obtained by considering the effect of hydrodynamic (oscillating inertial) flows around a plate without an acoustic baffle. Hydrodynamic flows allow fluid to escape compression, thereby reducing sound radiation, particularly at low frequencies at which the fluid has more time to escape compression.

The subcritical unbaffled plate radiation efficiency is given by

$$\sigma_{unb} = F_{plate}(F_{corner}\sigma_{corner} + F_{edge}\sigma_{edge}), \qquad f < f_c, \tag{5}$$

in which F_{plate} is a plate correction that accounts for the effect of inertial flows that surround the plate at low frequencies where the acoustic wavelength exceeds the dimensions of the plate, and the local corrections F_{corner} and F_{edge} account for the effect on radiation from corner and edge modes at higher frequencies due to localized inertial flows near the plate perimeter. The correspondence between terms in equation (5) and the radiating regions of

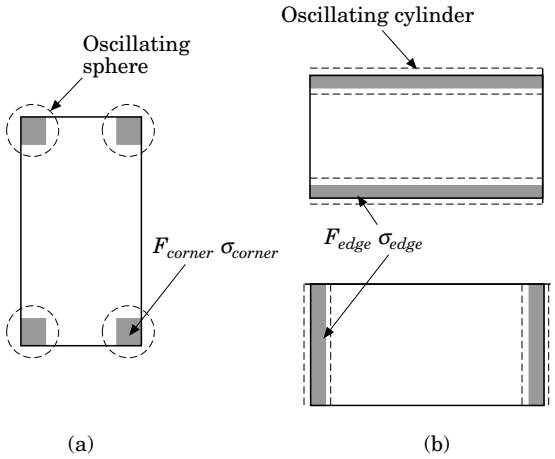

Figure 1. Dominant radiating regions of a baffled plate (shaded), and oscillating source representation (dashed lines) of unbaffled plate radiation. (a) Corner radiation is represented by oscillating spheres, and (b) edge radiation is represented by oscillating cylinders. Radiation from each region is described by the product of a baffled plate radiation efficiency σ_k and a correction factor F_k.

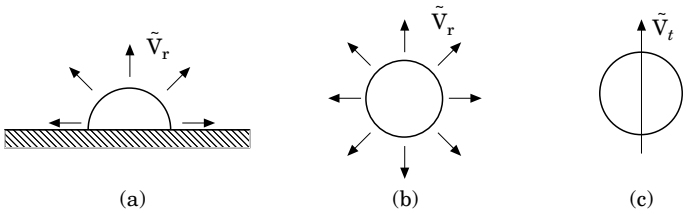

Figure 2. Representation of baffled and unbaffled radiating regions: (a) pulsating baffled source with radial velocity amplitude $\tilde{V}_r$, (b) equivalent representation of pulsating baffled source, (c) oscillating source with translational velocity amplitude $\tilde{V}_t$.

a plate is shown in Figure 1: contributions by corner modes are represented by term $F_{corner}\sigma_{corner}$, and contributions by edge modes are represented by term $\sigma_{edge}F_{edge}$. The derivation of the unbaffled plate radiation efficiency and the corrections F_{plate}, F_{corner}, and F_{edge} are discussed in the following.

The oscillatory inertial flow factors F_{corner} and F_{edge} in equation (5) multiply a radiation efficiency obtained from the simply supported baffled plate model. It is convenient to introduce the following form:

$$\sigma_{k,\,unb} = F_k\sigma_{k,\,baf}, \tag{6}$$

in which subscript k refers to *corner*, *edge*, or *plate*. In the following discussion the factors are presented according to the size of the region in which radiation-reducing flow occurs.

2.2.1. *The local corrections*

The corrections F_{corner} and F_{edge} describe the effects of localized flow in the vicinity of the perimeter of an unbaffled plate. Corner and edge corrections are introduced for the corner and edge regions that are largely responsible for sound radiation from a simply supported baffled plate; see Figure 1. No local correction is introduced for the so-called surface modes because these modes radiate from the entire plate surface [1, 8] and are therefore assumed to be affected negligibly by local flows.

Consider the removal of the baffle from a plane-baffled plate. With the baffle present, corner and edge modes radiate from both sides of the plate like pulsating spherical and cylindrical sources located next to the plate perimeter. With the baffle removed, fluid flow couples pairs of these oppositely phased sound sources on opposing sides of the plate, and oscillating sources are formed. The transition from a baffled plate to an unbaffled plate may therefore be modeled by replacing pulsating sources by oscillating sources, as suggested in reference [16]. Spherical sources are used for the corner regions, and cylindrical sources are used for edge regions, as indicated in Figure 1. Identical radii are used for corresponding pulsating and oscillating sources because the size of the radiating corner and edge regions is independent of baffling.

A local correction is related to the sound power ratio of oscillating and pulsating sources:

$$F_{local} = \tfrac{1}{2}\left(\frac{\Pi_{osc}}{\Pi_{pul}}\right). \tag{7}$$

The factor of 1/2 arises because radiation efficiency is inversely proportional to radiating surface area, which doubles in going from a one-sided baffled plate to a two-sided unbaffled plate; see equation (1). The sound power ratio Π_{osc}/Π_{pul} is found using the

modeling scheme shown in Figure 2. A radiating baffled corner or edge region is represented by a pulsating source with a semi-circular profile and uniform radial velocity amplitude $\tilde{V}_r$; see Figure 2(a). The tilde in $\tilde{V}_r$ denotes a complex quantity with magnitude and phase. The semi-circular source is acoustically equivalent to the pulsating source in Figure 2(b) which has a circular profile and the same uniform surface normal velocity $\tilde{V}_r$. The circular and semi-circular sources are equivalent because they both satisfy the baffled boundary condition, namely surface normal velocity $\tilde{V}_\perp = 0$ on the plane baffle and $\tilde{V}_\perp = \tilde{V}_r$ on the source above the plane baffle. Unbaffled corner or edge sources are modeled using an oscillating source with circular profile and translational rigid body velocity amplitude $\tilde{V}_t$ as shown in Figure 2(c).

Expressions for Π_{osc}/Π_{pul} are obtained by casting descriptions of low and high frequency behavior into a convenient analytical form. At high frequencies radiated power depends on the surface average of the square of normal velocity $\langle v^2 \rangle$ [11, 21], and the power ratio is taken with equal mean square velocities: $\langle v_{pul}^2 \rangle = \langle v_{osc}^2 \rangle$. The local correction at high frequencies is taken as unity because the radiated poser of pulsating and oscillating sources is approximately the same for equal $\langle v^2 \rangle$, as will be seen below. At low frequencies radiated power depends on displaced volume [21], and the ratio is evaluated for compact pulsating and oscillating sources with equal volume velocity magnitudes, $|\tilde{Q}_{pul}| = |\tilde{Q}_{osc}|$. Here, $\tilde{Q}_{pul}$ is the volume velocity amplitude displaced by the pulsating source in Figure 2(b), and $\tilde{Q}_{osc}$ is the volume velocity amplitude displaced by one side of the oscillating source in Figure 2(c). The correction factor thus has the form

$$F_{local} = \frac{1}{2} \times \begin{cases} x(ka), & ka \ll 1, \\ 1, & ka \gg 1, \end{cases} \tag{8}$$

in which x is a function of the acoustic wave number $k = \omega/c$, and the radius a of the pulsating or oscillating source is indicative of the effective separation between the actual source pairs on opposing sides of the plate. The low and high frequency limits of equation (8) are found in the function

$$F_{local} = \tfrac{1}{2}[x(ka)/(1 + x(ka))] \,. \tag{9}$$

The source radius a is related to the size of the efficiently radiating corner or edge region. The size of a radiating region for a plate mode is related to the wave number components $k_{m,x}$ and $k_{m,y}$ of mode shape ψ_m:

$$\psi_m = 2 \sin (k_{m,x}x) \sin (k_{m,y}y) = 2 \sin (n_x \pi x/l_x) \sin (n_y \pi y/l_y), \quad n_x, n_y = 1, 2, \ldots, \tag{10}$$

in which l_x and l_y are the length and width of the plate. The radius a is assumed to be proportional to a representative structural wavelength $\bar{\lambda}$:

$$a = \epsilon \bar{\lambda} = 2\pi\epsilon/\bar{k}_m(k_{m,x}, k_{m,y}), \tag{11}$$

in which the representative modal wave number $\bar{k}_m$ is a function of modal wave number components, and ϵ is a proportionality factor whose value is determined empirically below. Substituting this relationship into equation (9) gives a local correction for plate mode m:

$$F^{\,m}_{local} = \tfrac{1}{2}[x(\epsilon^2\alpha_m^2)/(1 + x(\epsilon^2\alpha_m^2))], \tag{12}$$

in which $\alpha_m = k/\bar{k}_m$.

The modal average unbaffled plate radiation of equation (5) is found by averaging modal unbaffled plate radiation efficiencies over the arc in wave number space that corresponds to the resonant plate response at frequency ω. The radius of the arc is given by the bending

wave number $k_b = (\omega/\kappa c_\ell)^{1/2}$ and spans both corner and edge mode regions, as shown in Figure 3:

$$\sigma_{unb} = F_{plate}\langle \sigma^m_{unb} \rangle_{k_m} = F_{plate}\langle F^m_{corner}\sigma^m_{corner,baf} + F^m_{edge}\sigma^m_{edge,baf} \rangle_{k_m}, \tag{13}$$

in which subscript k_m indicates an average over plate modal wave number. To carry out the modal average, the summation over modes in the averaging operation is replaced by an integration over wave number space, the assumption being that the density of plate modes is large enough to provide a good approximation. The plate correction F_{plate} is factored out from the averaging operation because it is at most weakly dependent on modal wave number, as will be seen below.

Having presented the general procedure for deriving local correction factors and unbaffled plate radiation efficiency, the discussion now specializes to the specific expressions for corner and edge radiating regions. To derive the corner correction, pulsating and oscillating spheres are used [21]:

$$\Pi_{pul} = \tfrac{1}{2}\rho_o c A_s[(ka)^2/(1 + (ka)^2)]|\tilde{V}_r|^2, \qquad \Pi_{osc} = \tfrac{1}{6}\rho_o c A_s[(ka)^4/(4 + (ka)^4)]|\tilde{V}_t|^2, \tag{14}$$

in which $\tilde{V}_r$ is the radial velocity amplitude of the pulsating sphere, $\tilde{V}_t$ is the translational rigid body velocity amplitude of the oscillating sphere, and $A_s = 4\pi a^2$ is the sphere surface area. At high frequencies, $ka \gg 1$, the sound power ratio is approximately unity with equal surface averaged squared normal velocities because $\langle v^2_{pul} \rangle = \frac{1}{2}|\tilde{V}_r|^2$ for the pulsating sphere and $\langle v^2_{osc} \rangle = \frac{1}{6}|\tilde{V}_t|^2$ for the oscillating sphere. At low frequencies, $ka \ll 1$, the sound power ratio is evaluated with equal volume velocities: $\tilde{Q}_{pul} = A_s\tilde{V}_r$ for the pulsating source and $\tilde{Q}_{osc} = \frac{1}{4}A_s\tilde{V}_t$ for the oscillating source. Following equation (11), radius a is related to a wave number that represents the size of an efficiently radiating corner region of plate mode m: $a = 2\pi\epsilon(k^2_{m,x} + k^2_{m,y})^{-1/2} = 2\pi\epsilon/k_b$. Here, $k_b = (\omega/\kappa c_\ell)^{1/2}$ is the bending wave number in which κ is the plate radius of gyration, and c_ℓ is the bulk speed of the plate. Radius a corresponds to the diagonal length of a corner region when $\epsilon = 1/4$. Equation (12) takes the form

$$F_{local} = F_{corner} = \tfrac{1}{2}\,[(16/3)\pi^2\epsilon^2\alpha^2/(1 + (16/3)\pi^2\epsilon^2\alpha^2)], \tag{15}$$

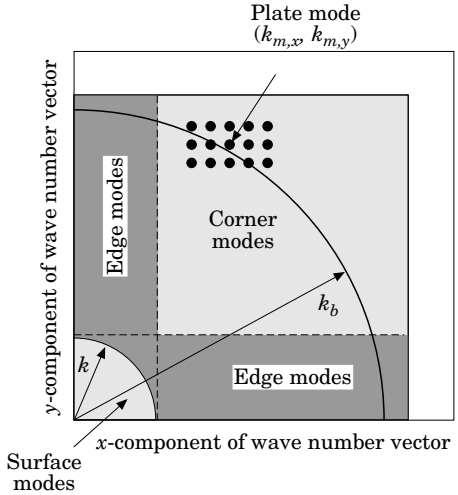

Figure 3. Wave number space for frequencies below plate critical frequency, after reference [1]. Each plate mode has a modal wave number vector ($k_{m,x}$, $k_{m,y}$). The relation of the wave number components to the acoustic wave number k and the bending wave number k_b acoustically classifies a plate mode as a corner, edge, or surface mode.

in which $\alpha^2 = f/f_c$, and superscript m has been omitted because the result is independent of modal wave number.

The derivation of the edge correction is similar to that for the corner modes except that cylindrical sources are used. The surface normal velocity on a cylinder is $\tilde{V}_\perp = \tilde{V}_n \cos(n\phi)e^{ik_z z}$, in which ϕ is the polar angle over the cylinder cross-section and k_z is the wave number along the cylinder axis. The value $n = 0$ corresponds to a pulsating cylindrical circular cross-section, and $n = 1$ corresponds to an oscillating cylindrical cross-section. The relevant quantity is sound power per length Π':

$$\Pi'_n = (\rho_o ck/\epsilon_n k_r^2 a|\mathrm{H}_n^{(2)\prime}(ka)|^2)|\tilde{V}_n|^2, \tag{16}$$

in which a is cylinder radius, $\mathrm{H}_n^{(2)\prime}(ka)$ is the derivative of the Hankel function of the second kind evaluated at ka, $k_r = \sqrt{k^2 - k_z^2}$, and $\epsilon_n = 0{\cdot}5$ for $n = 0$ and $\epsilon_n = 1$ for $n \geqslant 1$ [11].

At high frequencies, $ka \gg 1$, the sound power ratio Π'_{osc}/Π'_{pul} evaluates to unity because the square of surface normal velocity averaged over time and radiating surface is $\langle v_{pul}^2 \rangle = \frac{1}{2}|\tilde{V}_0|^2$ for the pulsating cylinder and $\langle v_{osc}^2 \rangle = \frac{1}{4}|\tilde{V}_1|^2$ for the oscillating cylinder. At low frequencies, $ka \ll 1$, the sound power per length of the pulsating and oscillating cylinders are [7]

$$\Pi'_0 = (\pi^2/2)\rho_0 ca(ka)|\tilde{V}_0|^2, \quad \Pi'_1 = (\pi^2/4)\rho_o ca(ka)^3|\tilde{V}_1|^2, \quad ka \ll 1. \tag{17}$$

After these expressions are written in terms of volume velocities per unit length, $\tilde{Q}'_{pul} = 2\pi a\tilde{V}_0$ for the pulsating cylinder and $\tilde{Q}'_{osc} = 2a\tilde{V}_1$ for the oscillating cylinder, the sound power ratio is taken with equal volume velocities. A wave number that approximately represents the width of edge regions is $\overline{k}_m \approx k_b$, the accuracy of which is best well below the plate critical frequency [22]. The edge correction follows:

$$F_{local} = F_{edge} = \tfrac{1}{2}[2\pi^4\epsilon^2\alpha^2/(1 + 2\pi^4\epsilon^2\alpha^2)], \tag{18}$$

which again is independent of modal wave number. Because the corner and edge corrections of equations (15) and (18) are independent of modal wave number, the modal averaging operation of equation (13) is a simple step and gives the subcritical unbaffled plate radiation efficiency of equation (5).

The value for the proportionality factor ϵ is obtained empirically by comparing predicted and measured data for a plate reported in the literature [18]. The plate measures $0{\cdot}3\ \mathrm{m} \times 0{\cdot}3\ \mathrm{m} \times 1{\cdot}22\ \mathrm{mm}$. Its critical frequency, at which acoustic and plate bending wave speeds are equal, is 10 200 Hz. Measured third octave band radiation data for this plate are considered in the subsequent discussions.

Radiation efficiencies for various values of ϵ are shown in Figure 4. The predictions are made using equation (5): the corner and edge corrections F_{corner} and F_{edge} are varied by changing ϵ, and no plate correction is applied ($F_{plate} = 1$). The figure shows reasonably good predictions of radiation efficiency from 500–5000 Hz for $\epsilon = 1/2$. Substituting this value into equations (15) and (18) gives

$$F_{corner} = \tfrac{1}{2}[13f/f_c/(1 + 13f/f_c)], \qquad F_{edge} = \tfrac{1}{2}[49f/f_c/(1 + 49f/f_c)]. \tag{19}$$

These local corrections suggest that the effect of localized flows on sound radiated from regions near the plate perimeter becomes important for frequencies well below critical, $f < f_c/13$, or $\lambda_b < 0{\cdot}28\lambda$ in terms of the plate bending and acoustic wavelengths.

The effective separation between the corner and edge regions on opposite plate sides are suggested by the source radius a. For $\epsilon = 1/2$, the radius is $\lambda_b/2$ in which λ_b is the plate bending wavelength. This compares with the value $\lambda_b/4$ hypothesized in reference [16].

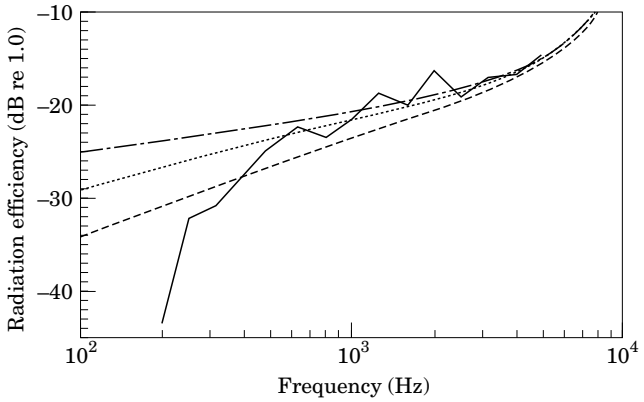

Figure 4. Effect of local corrections as a function of proportionality factor ϵ for a 0·3 m × 0·3 m × 1·22 mm unbaffled plate: ——, measured data; – – – – –, $\epsilon = 0{\cdot}25$; . . . . . , $\epsilon = 0{\cdot}5$; — — — — —, $\epsilon = 1$. Measurements from reference [18].

2.2.2. *The plate correction*

At low frequencies where the acoustic wavelength exceeds plate dimensions, inertial flows occur over a region that envelops the plate. The effect of these flows is described by the plate correction. The plate correction for unbaffled plates is obtained by considering the low frequency radiation of an oscillating sphere [15]:

$$F_{plate} = \tfrac{1}{12}(kb)^4, \quad kb \ll 1, \tag{20}$$

in which b is the sphere radius and is obtained by equating radiating surface areas of the sphere and plate, $b = \beta(A/2\pi)^{1/2}$, in which A is the one-sided area of the plate.

The plate correction is modified in two ways in this paper. First, a parameter β is introduced that multiplies the sphere radius b. Second, instead of applying the plate correction in a piecewise manner, the low frequency limit in equation (20) is incorporated into an expression with the form of equation (9), giving a smooth function of frequency. The resulting plate correction is

$$F_{plate} = \beta^4 k^4 A^2/48\pi^2/(1 + \beta^4 k^4 A^2/48\pi^2). \tag{21}$$

The effect of varying the proportionality factor β is shown in Figure 5. The plate correction F_{plate} is varied by changing β while the corner and edge corrections of equation (19) are applied. The value $\beta = 1$ has been used implicitly in reference [15], but $\beta = 2$ provides better accuracy. Substituting this value into equation (21) gives

$$F_{plate} = 53f^4 A^2/c^4/(1 + 53f^4 A^2/c^4). \tag{22}$$

The effect of the plate correction becomes important at low frequencies where $53f^4A^2/c^4 = 1$ or $\lambda/\sqrt{A} = 2{\cdot}7$, in which λ is the acoustic wavelength. This corresponds to a dimensionless wave number of $k\sqrt{A} = 2{\cdot}3$, where k is the acoustic wave number.

Having presented the unbaffled plate radiation efficiency and the local and plate corrections that it contains, its accuracy relative to other models is discussed next.

3. ASSESSMENT OF THE UNBAFFLED PLATE RADIATION EFFICIENCY

In this section the unbaffled plate radiation efficiency developed above is assessed against measured data, predictions by the simply supported baffled plate model, and a model of

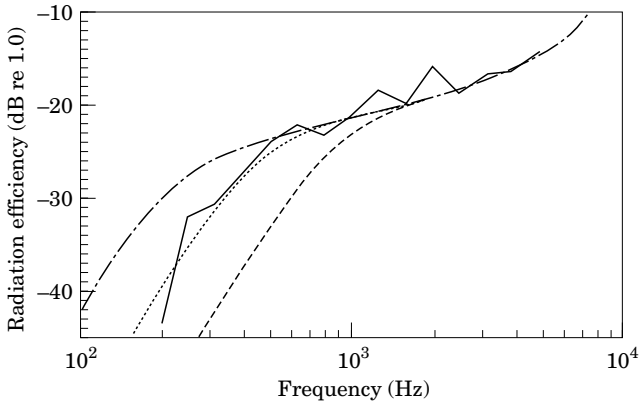

Figure 5. Effect of plate correction as a function of proportionality factor β for a 0·3 m × 0·3 m × 1·22 mm unbaffled plate: ——, measured data; – – – – –, $\beta = 1$; . . . . . , $\beta = 2$; — — — — —, $\beta = 4$. Measurements from reference [18].

sound radiated by bending waves normally incident on a plane-baffled free edge of a plate. The unbaffled plate radiation efficiency σ_{unb} of equation (5) accounts for the radiation-reducing effects of oscillating inertial flow. The baffled plate expression σ_{plate} of equation (2), based solely on the simply supported plane-baffled plate model, does not. The radiation efficiency of the baffled free edge model for frequencies well below critical is [14]

$$\sigma_{baf,free} = \tfrac{2}{5}(f/f_c)^2\sigma_{plate}. \tag{23}$$

Figure 6 shows a comparison of unbaffled plate, baffled (simply supported) plate and baffled free edge radiation efficiencies for the unbaffled plate considered in the previous section. The unbaffled predictions generally follow the frequency dependence of the measured data and are 3–20 dB more accurate than baffled predictions except at 1250 and 2000 Hz where baffled predictions are 1–3 dB more accurate. Improvements in accuracy above 800 Hz where $13f/f_c \approx 1$ result largely from the local corrections which reduce

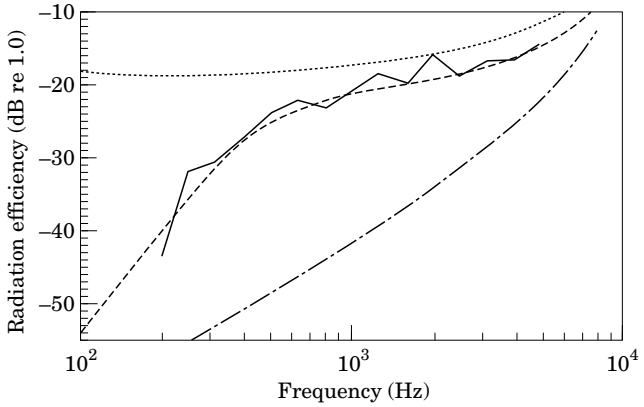

Figure 6. Improvement in predicted radiation efficiency for 0·3 m × 0·3 m × 1·22 mm unbaffled plate: ——, measured data; – – – – –, unbaffled; . . . . . , baffled supported; — — — —, unbaffled supported. Measurements from reference [18].

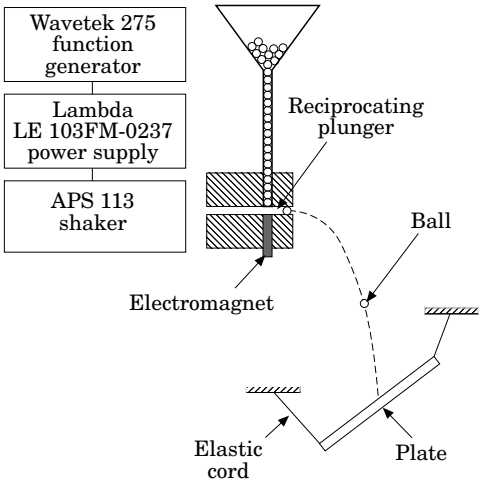

Figure 7. Schematic of ball drop system.

radiation efficiency by roughly one-half (3 dB). Greater improvements below 400 Hz where $53f^4A^2/c^4 \approx 1$ are due to both the local and plate corrections.

Unbaffled predictions are also seen to be more accurate than those of the baffled free edge model. Baffled free edge predictions range 6–24 dB lower than both measured data and unbaffled predictions. The degree of underprediction is surprising, as one might expect removal of the plane baffle to decrease sound radiation further.

4. EXPERIMENTAL VERIFICATION

To validate further the unbaffled radiation efficiency developed in Section 2, sound radiated by impacts between balls and a plate is examined. Measured data are compared with predictions obtained using the unbaffled, baffled simply supported, and baffled free edge radiation efficiencies. Sound radiated by non-propagating plate vibrations near ball-plate impact points is also considered. Impact and plate response predictions, which are necessary prior steps for sound radiation prediction, are done through established methods.

A schematic of the ball drop system is shown in Figure 7. Balls are expelled periodically from a hopper and fall onto an inclined plate. The steel balls measured 9·53 mm diameter, were expelled at a rate of 2 Hz, and attained a velocity component of 3·9 m/s normal to the plate prior to impact. The balls fell on one of two aluminum plates. One plate measured 0·4 m in length, 0·32 m in width, and 6·35 mm in thickness. The second had the same length and width but was 12·7 mm thick. The plates were supported at the corners by elastic cords. Felt was applied to each plate to provide damping. The loss factor of the fundamental mode on each plate was measured by the decay method. For the thin plate the loss factor was measured at 0·012; for the thick plate it was measured at 0·0055. The sound power radiated by the ball drop system was inferred from a ten point spatial average of sound pressure in a room of known reverberation time.

The vibration and sound power radiation of the ball drop system is predicted as follows. The normal impact force between the plate and the balls is obtained using the dynamic model shown in Figure 8 [10, 23]. In this model, a ball is represented as a rigid mass m, an idealization well approximated below the fundamental ball resonance. The contact stiffness between a ball and the plate is represented by a spring with rate k. The spring

rate was estimated at $k = 30 \times 10^6$ N/m by linearizing an expression for Hertzian contact stiffness [23]. The dynamics of the plate at the impact point are idealized by a dashpot with resistance equal to the plate drive point impedance $R_\infty = 4\rho_s c_\ell h^2/\sqrt{3}$, in which ρ and h are the plate density and thickness, and c_ℓ is the speed of compression waves in the plate. Using this dynamic model an equation for the force $\ell(t)$ between a ball and a plate can be written [10, 23]:

$$\ddot{\ell} + 2\zeta\omega_b\dot{\ell} + \omega_b^2\ell = 0, \tag{24}$$

along with initial conditions $\ell(0) = 0$ and $\dot{\ell}(0) = kv_o$ in which v_o is the velocity of the ball prior to impact. In this equation, $\omega_b = \sqrt{k/m}$ is the bounce frequency of a ball against an infinitely thick plate, and $\zeta = \sqrt{km}/2R_\infty$ is a rebound indicator; the balls rebound when $\zeta < 1$.

The force pulse due to one impact is obtained by solving equation (24) and zeroing the force $\ell(t)$ at times after it first becomes zero. The impact force spectral density $W_\ell(f)$ due to a periodic train of force pulses is then given by [10]

$$W_\ell(f) = 2v|L(2\pi f)|^2, \tag{25}$$

in which v is the rate of impact, and $L(\omega)$ is the Fourier Transform of the force pulse, and $\omega = 2\pi f$ [10, 23]:

$$\frac{|L(\omega)|^2}{(mv_0)^2} = [(1 - \Omega^2) + 4\zeta^2\Omega^2]^{-1}\begin{cases} 4e^{-\pi\beta}|\cos[(\pi/2)(\Omega_d - i\beta)]|^2, & \zeta < 1, \\ 1, & \zeta \geqslant 1, \end{cases} \tag{26}$$

in which

$$\Omega = \omega/\omega_b, \quad \Omega_d = \Omega(1 - \zeta^2)^{1/2}, \quad \beta = \zeta(1 - \zeta^2)^{-1/2}. \tag{27}$$

The average of the squared normal plate velocity, taken over time and the plate surface, is related to the impact force by [10]

$$\langle v^2\rangle = |H|^2\langle\ell^2\rangle = \langle\ell^2\rangle/R_\infty R = \int_{\Delta f} W_\ell(f)\,df/R_\infty R \approx W_\ell(f)\,\Delta f/R_\infty R, \tag{28}$$

in which $\langle\ell^2\rangle$ is the time average of the squared impact force in frequency band Δf, $|H|^2 = \langle|V/L|^2\rangle$ is the squared magnitude of the plate frequency response function averaged over drive (impact) point and response point, and $R = \eta\omega M$ is the average resistance of plate modes, M being the plate mass and η the average plate loss factor over frequency band Δf. The average over response points in $|H|^2$ is appropriate because the sound power radiation is, to a good approximation, proportional to the surface average of the square of velocity by equation (1). The average over the drive points is appropriate because more than 40 spatially distributed ball-plate impacts occurred during a

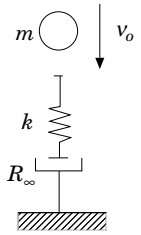

Figure 8. Dynamic impact model of ball and plate.

measurement; the majority of these occurred in a central region with roughly one-third of the plate area.

A comparison between the radiated power of the plate and the balls has shown that the contribution of the balls is negligible, largely because of the small ratio (0·0048) of surface areas of a ball to the plate [23]. The sound power radiated by the ball drop system is thus closely approximated by the power contribution of its plate:

$$\Pi = \rho_o c \sigma S \langle v^2 \rangle, \tag{29}$$

in which $S = 2A$ is the radiating surface area of the plate, and σ is a radiation efficiency. The radiation efficiency used for the ball drop system is

$$\sigma = \min(\sigma_0, 1), \tag{30}$$

in which min( ) returns the minimum of its arguments, and σ_o is either the unbaffled radiation efficiency σ_{unb} of equation (5), the baffled radiation efficiency σ_{baf} of equation (2), or the baffled free edge radiation efficiency $\sigma_{baf,free}$ of equation (23). The unity value in equation (30) is the high frequency limit of radiation efficiency for a simply supported baffled plate [1]. The radiation efficiency defined in equation (30) omits a description of increased radiation near the critical frequency, which can occur for plates with larger ratios of length to thickness than those considered in this study [5].

Sound radiated by non-propagating (near field) plate vibrations around the impact points is also considered. The sound power radiated from one side of an infinite plate excited by a normally applied force ℓ is [11]

$$\Pi_\infty = (\rho_o / 2\pi\rho_s h^2 c_\ell) \langle \ell^2 \rangle, \qquad f < f_c, \tag{31}$$

in which ρ and h are the plate density and thickness, and c_ℓ is the speed of compression waves in the plate. In the ball drop system a structural near field radiates sound from both sides of a plate, radiating power

$$\Pi_{nf} = 2\Pi_\infty. \tag{32}$$

This relation, being an infinite plate result, does not account for the effects of the free edge boundary conditions and finite self-baffling of the plate in the ball drop system. Hydrodynamic flows that couple the structural near fields on both sides of the plate are expected to reduce sound power radiation relative to equation (32), especially at low frequencies where the acoustic wavelength is larger than the plate dimensions.

Predictions of sound power radiated by the ball drop system with 6·35 mm and 12·7 mm thick plates are compared to measured one-third octave band data in Figures 9 and 10. Predictions are made using the unbaffled plate radiation efficiency, the baffled (simply supported) plate radiation efficiency, the baffled free edge radiation model, and the model of sound radiation from the structural near field. Predictions by the unbaffled and baffled plate radiation efficiencies coincide at high frequencies but differ at low frequencies, splitting near the critical frequency f_c which is 2000 Hz for the thin plate and 1000 Hz for the thick plate. Sound radiation is greatest at frequencies above critical, due to efficiently radiating surface modes which radiate from the entire plate surface [1, 8]. At supercritical frequencies the radiation efficiency is well predicted by the unity value associated with surface mode radiation from baffled plates well above the plate critical frequency. Surface mode radiation is thus minimally affected by inertial flows, and the two plate sides radiate independently, as has been assumed above and is consistent with previous findings [1].

The near field model generally underpredicts sound power radiation by the ball drop system, especially for the thicker plate. Underprediction ranges from 0–10 dB for the thin plate and 3–15 dB for the thick plate. The role of the near field contribution appears to

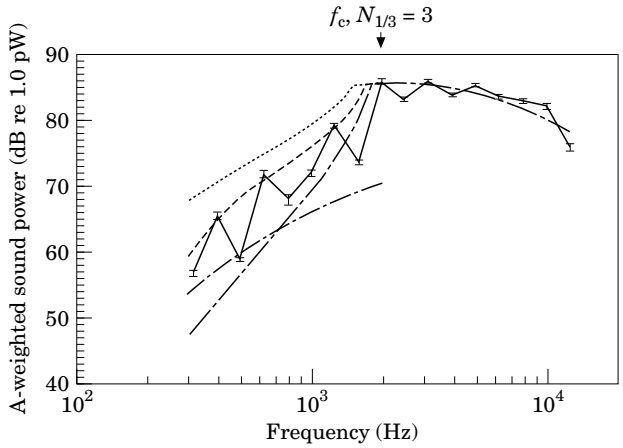

Figure 9. Measured and predicted sound power for ball drop system with 6·4 mm thick plate: —— , measured data; – – – – –, unbaffled; . . . . . , baffled supported; — – — – —, baffled free; – · – · –, near field. Plate critical frequency f_c and frequency above which one-third octave band mode count $N_{1/3}$ exceeds three are indicated.

be relatively minor, contributing importantly only to third octave bands with low levels of sound radiation.

The baffled free edge predictions are comparable to the unbaffled predictions. For the thin plate, unbaffled predictions tend to be more accurate at the lowest frequencies but less accurate at higher frequencies, and frequency dependence is suggested better by the unbaffled predictions. For the thick plate, the baffled free edge predictions are 2–5 dB more accurate, and the unbaffled and baffled free edge predictions show comparable frequency trends. This contrasts with the situation for the unbaffled plate discussed in Section 3 for which unbaffled predictions were 6–24 dB more accurate than baffled free edge predictions. The unbaffled radiation efficiency is thus more versatile than the baffled free edge model, at least for the three plates considered here, as can be seen by examining Figures 6, 9, and 10.

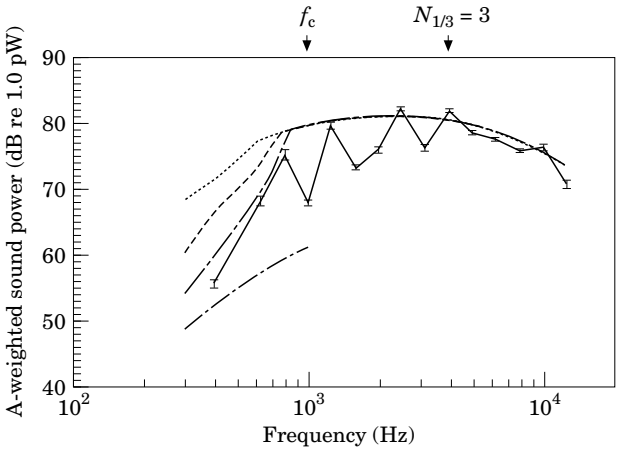

Figure 10. Measured and predicted sound power for ball drop system with 12·7 mm thick plate: —— , measured data; – – – – –, unbaffled; . . . . . , baffled supported; — – — – —, baffled free; – · – · –, near field. Plate critical frequency f_c and frequency above which one-third octave band mode count $N_{1/3}$ exceeds three are indicated.

Below the critical frequency, unbaffled predictions are more accurate than baffled predictions and better reflect the frequency trend of the measured data. Accuracy improvements range 3–9 dB, with a 3–6 dB improvement over most of the subcritical range. 3 dB of the improvement occurs from scaling the unbaffled radiation efficiency for two-sided instead of one-sided plate surface radiation; see equation (7). The remaining improvements are due to modeled inertial flow effects. The acoustic effect of flows that surround the plates is important below 360 Hz, where $53f^4A^2/c^4 \approx 1$ for both the thin and thick plates (which have equal surface areas). Local flows have a negligible effect on sound radiated by both plates over the measured frequencies; equation (19) suggests that radiating regions near the plate perimeter remain uncoupled by local flows for frequencies $f > f_c/13$, namely 150 Hz for the thin plate and 75 Hz for the thick plate.

The accuracy of the unbaffled predictions generally improves as frequency increases. Below 2000 Hz the local minima of the power radiated from the thin plate are overpredicted by 6–10 dB, and the local maxima are predicted within 1 dB. Accuracy within 3 dB is reached at 2000 Hz and above. Similar trends occur for the thick plate. Measured data are overpredicted by 4–12 dB below 1000 Hz. Between 1000 and 2000 Hz local maxima are predicted within 2 dB, and local minima are overpredicted by 5–12 dB. Consistent ± 3 dB accuracy is reached at 4000 Hz and above.

These accuracies are good in view of the low density of resonant modes in the plates. The expected mode count in a third octave band is $N_{1/3} = n(f)\Delta f$, in which $n(f) = 1{\cdot}7A/hc_\ell$ is the (expected) plate modal density and $\Delta f \approx 0{\cdot}23f_o$ is the width of a third octave band with center frequency f_o [11]. The one-third octave band mode count is small at low frequencies—0·6 for the thin plate and 0·3 for the thick plate in the 400 Hz band—and increases with frequency due to the increasing width of the third octave bands. The mode count exceeds three at 2000 Hz and above for the thin plate and at 4000 Hz and above for the thick plate. These frequencies correlate well with the transition to consistent 3 dB accuracy seen in Figures 9 and 10.

The effect of mode count on prediction accuracy arises from the statistical nature of the modeling approach. In the derivations of the impact model, the plate response model, and the unbaffled radiation efficiency, an average of response and sound radiation by resonant plate modes is considered, and therefore the number of resonating modes per frequency band is important. Accurate prediction of the mode count is more difficult when the mode count is low. At low frequencies the actual mode count is likely to be either zero or one, not a fraction as suggested by the expected mode count. Similarly, the one mode resonating in a band is either a corner or edge mode, not a fraction of each as equation (2) suggests. Moreover, the impact and plate response models are likely to be more accurate at high frequencies as the bending wavelength shortens relative to the plate region where impacts occur.

Another source of prediction error lies in the local and plate corrections contained in the unbaffled radiation efficiency. The corrections evaluate the effects of inertial flows in a simple approximate fashion, as opposed to a detailed evaluation of inertial flow effects based on the plate surface vibration distribution. Moreover, the proportionality factors contained in the corrections have been empirically obtained through comparison against only one plate. In spite of this simple approach, the modeling approach with the corrected radiation efficiency is able to predict the sound radiated by unbaffled plates with reasonable accuracy, even for plates with low mode counts.

The uncertainty in sound power radiated by the ball drop system may roughly be quantified using a statistical approach. The mean and variance of radiated sound power is determined, and a confidence interval is computed based on an assumed statistical distribution which uses these statistics as parameters. To compute the variance of sound

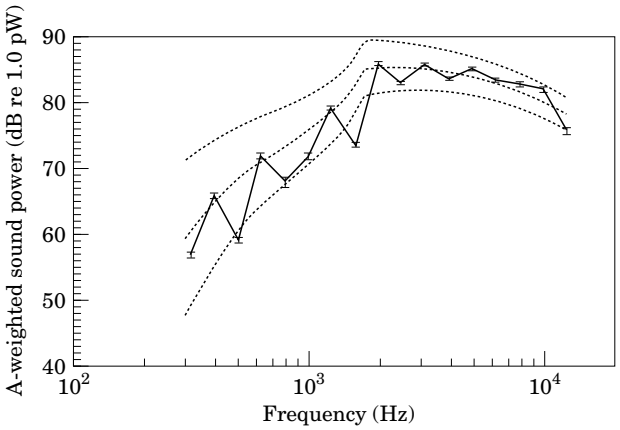

Figure 11. Comparision of 80% confidence interval against measured sound power of ball drop sytsem with 6·4 mm thick plate: ——, measured data; . . . . . , predicted mean and 80% confidence interval.

power radiation, the viewpoint is taken that plate resonance frequencies are not known and are treated as a random variable. It is assumed that the sound power variability is largely due to a sensitivity of plate response to frequency, and that the effect of impact force variability is negligible.

Using these assumptions the mean μ_Π and variance s_Π^2 of sound power radiation are found using equations (28) and (29):

$$\mu_\Pi = \sigma\rho cS\langle\ell^2\rangle\mu_{|H|^2}, \qquad s_\Pi^2 = [\sigma\rho cS\langle\ell^2\rangle]^2 s_{|H|^2}^2, \tag{33}$$

in which $\mu_{|H|^2}$ and $s_{|H|^2}^2$ are the mean and variance of the plate response function $|H|^2 = \langle|V/L|^2\rangle$, which is averaged over drive and response points. Using the methods developed in reference [19], the normalized variance of $|H|^2$ can be shown to be

$$w_{|H|^2} = s_{|H|^2}^2/\mu_{|H|^2}^2 = 2[1 + 1/2M]F(Q)/Q, \tag{34}$$

in which M is plate modal overlap, Q is specific bandwidth, and $F(Q)$ is given by

$$F(Q) = (2/\pi)[\tan^{-1}(\pi/2) - (1/\pi Q)\ln(1 + \pi^2Q^2/4)]. \tag{35}$$

The modal overlap M is the ratio of the effective modal bandwidth $\pi\eta\omega/2$ to the modal separation $1/n(\omega)$, in which $n(\omega)$ is the modal density (modes per radian frequency). The specific bandwidth Q is the lesser of the excitation and analysis bandwidths divided by effective modal bandwidth; for the ball drop system broad band impact sound is examined in one-third octave bands and $Q = 0{\cdot}46/\pi\eta$. Equation (34) is independent of impact and response location, which would appear as spatial moments of plate mode shape, because these dependencies have been averaged out of the response function $|H|^2$.

Confidence intervals for radiated power are found by assuming the plate response to be gamma distributed. The gamma probability distribution has been shown to be exact for systems with large modal overlap and is assumed to be approximate for smaller modal overlap values [19]. The confidence coefficient CC is the probability that the surface average of plate response resulting from impacts uniformly distributed over the plate falls within a factor of r of the mean response, which is given by equation (28):

$$CC = \Gamma(u)^{-1}[\gamma(u, ru) - \gamma(u, u/r)], \tag{36}$$

in which $\Gamma(u)$ is the gamma function, $\gamma(u, x)$ is the incomplete gamma function, and $u = 1/w$ is the reciprocal of normalized variance [19].

In Figure 11 measured sound power data is compared to an 80% confidence interval found by numerically inverting equation (36). The 80% confidence interval is the factor r, expressed in dB, that is expected to capture 80% of the measured values. The portion of data contained in the confidence interval would be expected to approach 80% as the amount of measured data increased, provided that both the modeling approach and the gamma distribution described above were accurate descriptors. In fact the confidence interval contains 15 of the 17 measured values, a fraction of 88%. To assess the performance of the confidence interval, the statistics of a process with an 80% chance of bounding each data point is examined using binomial distribution [24]. The probability of bounding 15 of the 17 data points is 19%; the most probable number of bounded data points is 14 and has a 23% chance of occurring. The performance of the confidence interval, which is based on a number of modeling and statistical assumptions, is thus encouraging but not conclusive due to the limited amount of measured data.

5. CONCLUSION

A corrected radiation efficiency for radiation below the critical frequency of plates has been developed and experimentally validated. The corrected radiation efficiency contains scaling factors whose values were chosen empirically by comparison with measured data.

The accuracy of the corrected radiation efficiency is encouraging. The corrected radiation efficiency provides better low frequency accuracy than a modal average radiation efficiency derived from the simply supported plane-baffled plate model while requiring minimal additional calculation. The prediction accuracy is also more consistent than predictions by a plane-baffled, free edge model. Improvement in accuracy typically ranges from 4–12 dB, with the greatest improvements occurring at low frequencies, where accuracy may be better by more than 20 dB.

ACKNOWLEDGMENTS

The authors gratefully acknowledge the support of the National Aeronautics and Space Administration under grant NGT-50364 and the National Science Foundation under grant MSM-8410530.

REFERENCES

1. G. Maidanik 1962 *Journal of the Acoustical Society of America* **34**, 809–826. Response of ribbed panels to reverberant acoustic fields.
2. I. L. Ver and C. I. Holmer 1971 *Noise and Vibration Control* 287–296. New York. McGraw-Hill Book Co. Interaction of sound waves with solid structures. (editor L. Beranek).
3. C. E. Wallace 1987 *Journal of the Acoustical Society of America* **81**, 1787–1794. The acoustic radiation damping of the modes of a rectangular panel.
4. M. Abom and H. Boden 1987 *Applied Acoustics* **22**, 203–212. A method for estimating the radiation from plates with prescribed excitation in the multi-mode region.
5. R. Timmel 1991 *Acustica* **73**, 1–11. The radiation efficiency of rectangular thin homogeneous plates in an infinite baffle.
6. M. K. Rahman, A. Ertas 1994 *Thin-Walled Structures* **18**, 3–22. Acoustic power radiation from rectangular plate with mixed boundary conditions.
7. F. Fahy 1985 *Sound and Structural Vibration*: *Radiation*, *Transmission*, *and Response*. London: Academic Press.
8. P. W. Smith and R. H. Lyon 1965 *NASA Technical Report CR*-160 Sound and structural vibration. Bolt, Beranek, and Newman, Inc.

9. C. E. Wallace 1972 *Journal of Acoustical Society of America* **51**, 946–952. Radiation resistance of a rectangular panel.
10. R. H. Lyon 1987 *Machinery Noise and Diagnostics*. Boston: Butterworths Publishers.
11. L. Cremer, M. Heckl and E. E. Ungar 1973 *Structure-Borne Sound*. Berlin: Springer-Verlag.
12. M. C. Gomperts 1977 *Acustica* **37**, 93–102. Sound radiation from baffled, thin rectangular plates.
13. R. H. Lyon 1963 *Journal of the Acoustical Society of America* **35**, 1791–1797. Noise reduction of rectangular enclosures with one flexible wall.
14. M. C. Gomperts 1974 *Acustica* **30**, 320–327. Radiation from rigid baffled, rectangular plates with general boundary conditions.
15. W. Schirmer 1979 *Noise Control Engineering Journal* **12**, 31–37. Engineering methods for measuring and computing the acoustical transmission of machine structures.
16. E. J. Richards, R. K. Westcott and R. K. Jeyapalan 1979 *Journal of Sound and Vibration* **65**, 419–451. On the prediction of impact noise part II: ringing noise.
17. E. G. Williams 1983 *Journal of the Acoustical Society of America* **74**, 343–347. Numerical evaluation of the radiation from unbaffled, finite panels using the FFT.
18. F. Fahy 1985 *Sound and Structural Vibration*: *Radiation*, *Transmission*, *and Response*, 71. London: Academic Press.
19. R. H. Lyon 1969 *Journal of the Acoustical Society of America* **45**, 545–565. Statistical analysis of power injection and response in structures and rooms.
20. A. J. Price and M. J. Crocker 1969 *Journal of the Acoustical Society of America* **47**, 683–693. Sound transmission through double panels using statistical energy analysis.
21. A. D. Pierce 1981 *Acoustics*: *An Introduction to its Physical Principles and Applications*. New York: McGraw-Hill Book Co.
22. R. H. Lyon and E. Eichler 1964 *Journal of the Acoustical Society of America* **36**, 1344–1354. Random vibration of connected structures.
23. C. H. Oppenheimer 1992 *PhD thesis*, *Department of Mechanical Engineering*, *Massachusetts Institute of Technology*, *Cambridge*, *MA*. Impact-Induced Noise and Vibration of Machine Systems for Design.
24. S. M. Ross 1984 *A First Course in Probability*. New York: MacMillan Publishing Co.